Hyperfine, rotational, and vibrational structure of the $a^3\Sigma_u^+$ state of $^{87}Rb_2$

C. Strauss,[1,2] T. Takekoshi,[1] F. Lang,[1] K. Winkler,[1] R. Grimm,[1] and J. Hecker Denschlag[1,2]
[1]*Institut für Experimentalphysik und Zentrum für Quantenphysik, Universität Innsbruck, A-6020 Innsbruck, Austria*
[2]*Institut für Quantenmaterie, Universität Ulm, D-89069 Ulm, Germany*

E. Tiemann
Institute of Quantum Optics, Leibniz Universität Hannover, D-30167 Hannover, Germany
(Received 10 September 2010; published 19 November 2010)

We have performed high-resolution two-photon dark-state spectroscopy of an ultracold gas of $^{87}Rb_2$ molecules in the $a^3\Sigma_u^+$ state at a magnetic field of about 1000 G. The vibrational ladder as well as the hyperfine and low-lying rotational structure are mapped out. Energy shifts in the spectrum are observed due to singlet-triplet mixing at binding energies as deep as a few hundred GHz $\times h$. This information, together with data from other sources, is used to optimize the potentials of the $a^3\Sigma_u^+$ and $X^1\Sigma_g^+$ states in a coupled-channel model. We find that the hyperfine structure depends weakly on the vibrational level. This provides a possible explanation for inaccuracies in recent Feshbach resonance calculations.

DOI: 10.1103/PhysRevA.82.052514 PACS number(s): 33.20.−t, 37.10.Pq, 37.10.Jk, 42.50.−p

I. INTRODUCTION

Recently, optical schemes have been developed to selectively produce cold and dense samples of deeply bound molecules in well-defined quantum states [1–3] (see also [4,5]). This has opened up new possibilities for cold collision experiments, ultracold chemistry [6–8], and testing fundamental laws via precision spectroscopy [9–11]. For such future experiments it is mandatory that the location and properties of the available molecular quantum states are well known and understood.

Until recently, the $a^3\Sigma_u^+$ triplet potential of the Rb_2 molecule had remained largely experimentally unexplored. Natural samples of Rb_2 are normally found in their $X^1\Sigma_g^+$ singlet state, from which the lowest triplet state is somewhat difficult to reach in an optical Raman process due to a change in u-g symmetry. Here we report precision spectroscopy of $^{87}Rb_2$ molecules in this lowest triplet state, $a^3\Sigma_u^+$ ($5S_{1/2} + 5S_{1/2}$), where we resolve vibrational, rotational, hyperfine, and Zeeman structure with an accuracy as high as 30 MHz. We use dark-state spectroscopy, where a gas of weakly bound Feshbach molecules is irradiated by two laser beams. Molecular losses, induced by one of the two lasers, are suppressed when the second laser is tuned into resonance with a bound state (see Fig. 1). Fitting a coupled-channel model to our experimental data, we have constructed an accurate Born-Oppenheimer potential for $a^3\Sigma_u^+$. This enables us to calculate the wave functions of triplet bound states as well as their binding energies to 60 MHz $\times h$ accuracy (where h is Planck's constant) over the whole manifold of vibrational and low rotational ($N < 5$) levels. Our theory and data agree to the extent that further refinement of the theoretical model requires a reduction in the experimental uncertainty.

Molecular spectroscopy with cold atomic gases goes back to the beginnings of laser cooling [12–14]. An experiment closely related to ours is the one by Araujo *et al.* [15], where the Na_2 triplet ground state was explored using a magneto-optical trap combined with two-color photoassociation spectroscopy. Our spectroscopy also makes use of a two-photon transition, but starts from cold Feshbach molecules rather than from free atoms. Recent investigations of the $a^3\Sigma_u^+$ potential of Rb_2 include the work of [16–18]. Using one-color photoassociation of the $a^3\Sigma_u^+$ potential of laser-cooled ^{85}Rb, Ref. [16] put tight constraints on the position of the repulsive wall of the $a^3\Sigma_u^+$ potential but was not able to resolve the vibrational structure. The two other groups determined several rovibrational levels using fluorescence spectroscopy [17] or pump-probe photoionization spectroscopy of Rb_2 formed on helium nanodroplets [18]. Our work goes well beyond these measurements as we fully resolve hyperfine, rotational, and Zeeman structure for almost all vibrational states. Highly precise data of the asymptotic behavior of the coupled $a^3\Sigma_u^+$-$X^1\Sigma_g^+$ system is contained in the large set of observed Feshbach resonances [19–22] and in the two-photon photoassociation measurements of four weakly bound levels at zero magnetic field by [23].

This article is organized as follows: Section II presents the experimental setup and typical dark-state spectroscopy scans. Section III discusses the relevant quantum numbers of our studies and the assignment of the observed lines. Section IV is a short summary of the coupled-channel model and the optimization procedure of the Born-Oppenheimer potentials. Section V discusses the progression of the substructure of the vibrational manifolds. We conclude the article with a summary and an outlook toward further experiments in Sec. VI.

II. EXPERIMENTAL SETUP AND DARK-STATE SPECTROSCOPY

The starting point for our experiments is a 50-μm-size pure ensemble of 3×10^4 weakly bound Feshbach molecules which have been produced from an atomic Bose-Einstein condensate of ^{87}Rb by ramping over a Feshbach resonance at a magnetic field of 1007.4 G (1 G $= 10^{-4}$ T) [24]. They are trapped in the lowest Bloch band of a cubic 3D optical lattice with no more than a single molecule per lattice site [25]. The lattice depth for the Feshbach molecules is 60 E_r, where $E_r = \pi^2\hbar^2/2ma^2$ is the recoil energy, with m the mass of the molecules and $a = 415.22$ nm the lattice period. Such deep lattices prevent the molecules from colliding with each other, which suppresses

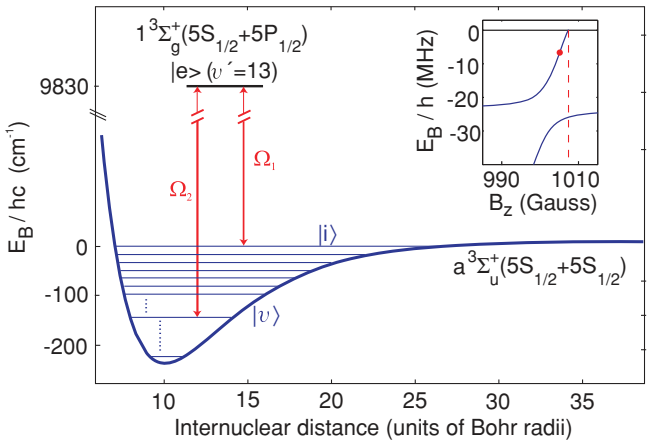

FIG. 1. (Color online) Dark-state spectroscopy scheme for the $^{87}Rb_2$ $a^3\Sigma_u^+$ potential. Lasers 1 and 2 couple the molecular levels $|i\rangle$ and $|v\rangle$ to the excited level $|e\rangle$ with Rabi frequencies $\Omega_{1,2}$, respectively. Laser 1 is kept on resonance while laser 2 can be tuned to any level of the $a^3\Sigma_u^+$ potential. (Inset) Bound-state level of Feshbach molecules as a function of magnetic field B_z. The dashed line gives the position of the Feshbach resonance. The dot marks the Feshbach molecule state used in the experiments.

collisional decay. We observe lifetimes of a few hundred ms. After producing the Feshbach molecules, the magnetic field is set to 1005.8 G, where the spectroscopy is carried out. At this magnetic field, the binding energy of the Feshbach molecules is 4.4(3) MHz $\times$ h (Fig. 1, inset).

Our dark-state spectroscopy works as follows: The Feshbach molecules in state $|i\rangle$ are irradiated by simultaneous rectangular pulses from lasers 1 and 2. The pulses typically last 10 μs with Rabi frequencies Ω_1 and Ω_2, respectively (Fig. 1). We keep laser 1 resonant with the $|i\rangle$–$|e\rangle$ transition and at a power I_1 of about 0.1 mW ($\Omega_1 = 2\pi \times 0.3$ MHz) such that in the absence of laser 2 about half of the molecules are lost by spontaneous emission from $|e\rangle$. Laser 2 with its power I_2 (up to a few hundred mW) is scanned. As long as laser 2 does not hit an $|e\rangle$–$|v\rangle$ resonance, laser 1 will continue to induce losses. However, when an $|e\rangle$–$|v\rangle$ resonance occurs, the initial state $|i\rangle$ is projected onto a dark state $|\Psi_{\text{dark}}\rangle = (\Omega_2|i\rangle - \Omega_1|v\rangle)/\sqrt{\Omega_1^2+\Omega_2^2}$. Molecules in this dark state are shielded from excitation to the short-lived level $|e\rangle$ [26]. This leads to a suppression of molecular losses. After the lasers are switched off we measure the number of molecules via a reverse magnetic field sweep through the Feshbach resonance, dissociating the remaining molecules in $|i\rangle$ into atoms which are detected by absorption imaging. These measurements are destructive, and for each point in a scan, a fresh sample of Feshbach molecules has to be prepared.

The level $|e\rangle$ has an excitation energy of about 295 THz $\times$ h with respect to $|i\rangle$ and a width $\Gamma = 2\pi \times 8$ MHz. Laser 1, a grating-stabilized diode laser, is Pound-Drever-Hall locked to a cavity which is in turn locked to an atomic ^{87}Rb line. Laser 2, a Ti:sapphire laser, is free-running and typically drifts over a frequency range of a few MHz within seconds. Both lasers have a short-term laser linewidth of several tens of kHz. Their beams have a $1/e^2$ intensity waist radius of 130 μm at the molecular sample, through which they propagate nearly collinearly. They are polarized parallel to the magnetic bias field B_z (pointing in the vertical direction) and thus can only induce π transitions. The frequencies of both lasers are automatically read out using a commercial wave meter (WS7 from HighFinesse). The binding energy E_B of $|v\rangle$ minus the binding energy of our initial Feshbach state (4.4 MHz $\times$ h) corresponds to the frequency difference of the two lasers. The wave meter has a nominal accuracy of 60 MHz after calibration. Over the course of days we have observed drifts of $\pm$200 MHz, for example, by repeatedly addressing the same spectroscopic line. Over the length of a few experimental cycles (5 min) the wave meter is stable to within 10 MHz, which represents a random noise floor. Assuming a sufficiently smooth behavior of the wave meter, drifts of the wave meter typically affect the frequency measurements of laser 1 and laser 2 in a similar way, especially since the laser frequencies only differ by 3%. Thus, such common mode drifts cancel out in the binding energy to first approximation. Indeed, based on our experience with the wave meter where we have measured binding energies of a few sharp lines over an extended period of time and via various intermediate levels we estimate the accuracy to reach 30 MHz. This includes peak position uncertainties due to variations of the number of molecules produced, as well as a frequency drift of laser 2 during the time between the laser pulse and wavelength measurement.

Figure 2(a) shows the measured binding energies of the triplet potential as a function of the vibrational quantum number v at a magnetic field of 1005.8 G. There are 41 vibrational states with binding energies ranging from 5 MHz $\times$ h to about 7038 GHz $\times$ h. The vibrational splitting between the two lowest vibrational levels, $v = 0$ and $v = 1$, is about 393 GHz. Each vibrational state has hyperfine, rotational, and Zeeman substructure. This structure is spread out over a range of about 20 GHz, as shown in Fig. 3 for the states $v = 0$ and 6. These spectra typically consist of roughly 1000 points corresponding

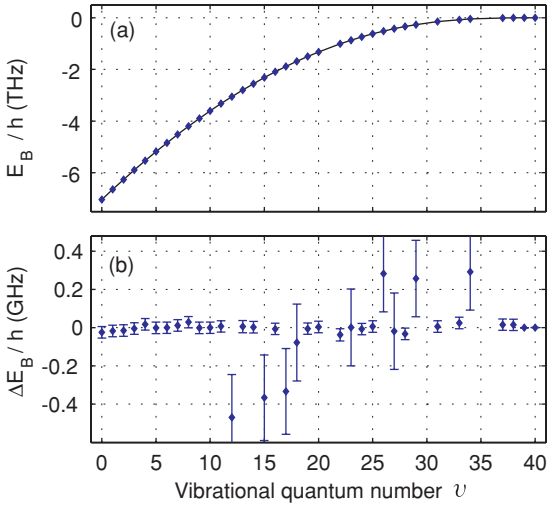

FIG. 2. (Color online) (a) Binding energies $E_B(v)$ for the state $a^3\Sigma_u^+$, where v is the vibrational quantum number. The line is the result of a coupled-channel model calculation after optimization of the Born-Oppenheimer potential. Five levels were not measured. (b) Residues, that is, the difference between experimental data and theory. Large error bars belong to early measurements without simultaneous wave-meter readings of both lasers.

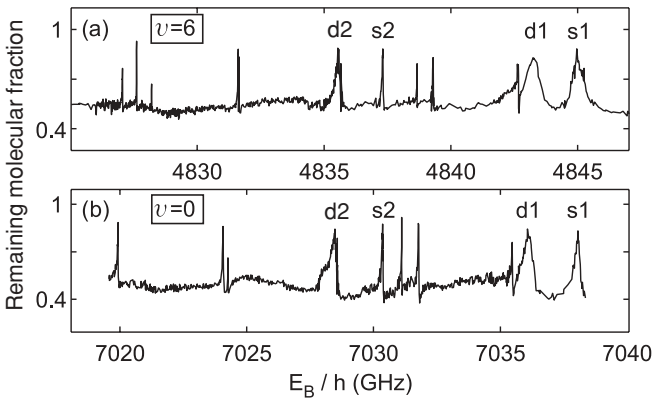

FIG. 3. Scans of two vibrational levels: (a) $v = 6$, (b) $v = 0$. Plotted is the remaining molecular fraction as a function of the binding energy E_B, which basically corresponds to the laser difference frequency. The scans were recorded using an excited state $|e\rangle$ with 1_g character. The labels s and d indicate rotational states $N = 0$ and 2, respectively. The numbers after the labels s or d indicate the position in the spectrum.

to an average step size of 20 MHz. Each point represents one production and measurement cycle which takes 28 s.

In each spectrum of Fig. 3 we observe some 10 lines which vary markedly in linewidth. The width of each line is determined by the coupling between the levels $|e\rangle$ and $|v\rangle$, that is, the Rabi frequency Ω_2. Interestingly, for our measuring scheme this width scales as Ω_2^2 [27] and not as Ω_2 [28,29], as one might expect. We have taken advantage of this enhanced broadening when searching for lines and vibrational manifolds, which otherwise can be like looking for a needle in a haystack. For example, for $v = 0$ and an intensity I_2 of a few hundred mW we reached linewidths of several GHz. The substructure of the desired vibrational level then appears essentially as a single broad line with a width of about 20 GHz. Once this level was found, the power was reduced in order to resolve its substructure.

In general, we expect spectra of different vibrational levels to be very similar. Up to $v = 35$ this is indeed the case. For $v \geqslant 35$ the vibrational manifolds start to overlap, as the splitting between them becomes smaller than 20 GHz. Spectra (a) ($v = 6$) and (b) ($v = 0$) of Fig. 3 are clearly similar. Some visible differences are artifacts; for example, it seems that in spectrum (b) two narrow lines are missing at $E_B/h \approx$ 7021 GHz. This can be explained by the fact that the lines were narrower (width $\leqslant$ 10 MHz) than the local step size of that scan and thus escaped observation.

III. QUANTUM NUMBERS AND ASSIGNMENT

A. Quantum numbers

For a deeper understanding of the structure of the spectrum and its assignment we now discuss the relevant quantum numbers and selection rules.

For the weakly bound levels like the Feshbach state or the vibrational levels close to the atomic asymptote, Hund's coupling case (e) with atomic quantum numbers is most appropriate. Here none of the angular momenta couple to the molecular axis. The state vector is described by

$$|(f_A, f_B) f, l, F, M\rangle,$$

where f_A, f_B are the total angular momenta for atoms A and B, f is the sum of both atomic angular momenta, l is the mechanical rotation of the atomic pair, F is the total angular momentum of the pair, and M is its projection onto a space-fixed axis. At low magnetic fields the prepared Feshbach state $|i\rangle$ can be approximated by the state vector $|f_A = 2, f_B = 2, f = 2, l = 0, F = 2, M = 2\rangle$. At the magnetic field used in the experiment (1005.8 G), F is no longer a good quantum number because of only weak coupling between l and f. A more appropriate state vector is

$$|(f_A, f_B) f, m_f, l, m_l, M\rangle.$$

M is a good quantum number, while for example, f_A and f_B have expectation values [30] of about 1.79 instead of quantum numbers $f_A = f_B = 2$ for 0 G.

Due to the strong hyperfine coupling of Rb and the large exchange energy, deeply bound levels of the triplet state can be described by Hund's coupling case (b_β) at low magnetic fields [31], namely,

$$|N, (I, S) f, F, M\rangle,$$

where I and S are the total nuclear and electronic spin quantum numbers, N the molecular rotation including electron orbital angular momentum, and F and M have exactly the same meaning as in Hund's case (e). The index β indicates that the nuclear spin I is not coupled to the molecular axis. Since both atoms are in the $5S$ configuration of Rb, the molecular electronic orbital angular momentum is zero. This means that $N = l$ and that f is the same as in Hund's case (e). Here we get

$$|N, m_N, (I, S) f, m_f, M\rangle,$$

as an appropriate state vector for higher magnetic fields, where $M = m_N + m_f$. One can show that owing to the antisymmetry of the molecular wave function with respect to nuclear exchange (nuclear spin of ^{87}Rb $i = \frac{3}{2}$), molecules with even (odd) N in the $a^3\Sigma_u^+$ state must have either a total nuclear spin $I = 1$ or 3 ($I = 0$ or 2) [31,32]. For the $X^1\Sigma_g^+$ singlet ground state this relation is reversed because it has g symmetry in contrast to the u symmetry of the triplet state. For large magnetic fields, f loses its meaning as S and I start to decouple.

Expectation values for the total nuclear spin and the electron spin for our Feshbach level are $I = 1.56$ and $S = 0.76$, respectively. Thus, we have significant electronic singlet-triplet mixing and consequently also mixing of the basis vectors with different I. In contrast, the excited intermediate state $|e\rangle$ has well defined quantum numbers S and I. Thus, $|e\rangle$ largely determines which quantum numbers the deeply bound $a^3\Sigma_u^+$ levels will have in the Raman transition.

The intermediate level $|e\rangle$ is located in the $v' = 13$ manifold of the $1^3\Sigma_g^+(5S_{1/2} + 5P_{1/2})$ potential. Due to significant effective spin-spin interaction, the vibrational manifold is split into two components, 1_g and 0_g^-, separated by 47 GHz. As intermediate level $|e\rangle$ we either choose a level with 1_g character or with 0_g^- character. Its rotational energy must be low because

the Feshbach level has the lowest rotational quantum number $N = 0$. As rotation is low in $|e\rangle$, decoupling of S and I from the molecular axis by rotation is not yet important. We can then approximate the state $|e\rangle$ by quantum numbers for Hund's case (a_α) where the index α indicates that the nuclear spin I is coupled to the molecular axis,

$$|S\Sigma, I\Omega_I, F, M\rangle.$$

The projections of the electronic and nuclear spin onto the molecular axis appear as quantum numbers Σ and Ω_I, respectively.

The $|e\rangle$ level with 1_g character is energetically the lowest within the $1_g(v = 13)$ manifold. It has the quantum numbers $S = 1$, $|\Sigma| = 1$, $I = 3$, $|\Omega_I| \approx 3$, $F \approx 2$, and $M = 2$ for low magnetic fields B_z. Its excitation energy is 294.626 4(2) THz $\times h$ with respect to $|i\rangle$ at a field of 1005.8 G.

The $|e\rangle$ level with 0_g^- character has an excitation energy of 294.673 6(2) THz. It can be described by the quantum numbers $S = 1$, $\Sigma = 0$, $I = 3$, $M = 2$, and $F = 3$ at $B_z = 0$. Because of its low hyperfine coupling, the better choice of basis vector here is

$$|S\Sigma, (JI)F, M\rangle,$$

where J results from the coupling of the electronic spin and the molecular rotation ($\mathbf{J} = \mathbf{N} + \mathbf{S}$). For our 0_g^- $|e\rangle$ level, J is approximately zero. Our 1_g $|e\rangle$ state is a superposition of $N = 1$ and 3.

As stated before, due to the laser polarization along the magnetic field, only π transitions are allowed, which results in the selection rule $\Delta M = 0$. Further, in a one-photon transition parity has to change. The Feshbach state $|i\rangle$ has a total parity "plus" because it is a Σ^+ state and $(-1)^N = 1$. Thus, we can only address $|e\rangle$ levels with "minus" parity and $|v\rangle$ levels with "plus" parity. This means that the $|v\rangle$ level must have an even rotational quantum number $N = 0,2,4,\ldots$. For the $|e\rangle$ level only quantum numbers $N = 1,3,\ldots$, or superpositions of these, are available. In fact, as the $1^3\Sigma_g^+$ state is well described in a Hund's case (a) basis, N is in general not a good quantum number for the $|e\rangle$ level. The selection rule $\Delta N = \pm 1$ for N determines the range of reachable levels for $|v\rangle$ according to the superposition in $|e\rangle$. The selection rules $\Delta I = 0$ and $\Delta S = 0$ are important for the transition $|e\rangle$ to $|v\rangle$. For the transition $|i\rangle$ to $|e\rangle$ they are, however, nearly irrelevant since I and S are not good quantum numbers for level $|i\rangle$.

B. Assignment of spectral lines

Figure 4 shows measured and calculated (based on the coupled-channel model, see Sec. IV) lines of the $v = 6$ spectrum, where the excited state $|e\rangle$ with 0_g^- character was selected. The lines form three groups with the quantum numbers $f = 4$, 3, and 2, according to the hyperfine coupling of $S = 1$ and $I = 3$. This is a clear indication that the hyperfine energy is still dominant compared to the Zeeman energy.

Each group consists of one line with $N = 0$ corresponding to a nonrotating molecule and several lines with $N = 2$ which are shifted to lower binding energy by about 2 GHz $\times h$ due to rotation. The fact that we do not observe lines with $N > 2$ can be explained as follows: The excited state $|e\rangle$ has "minus" total parity. Since $J = 0$ and $S = 1$, N must be equal to one and

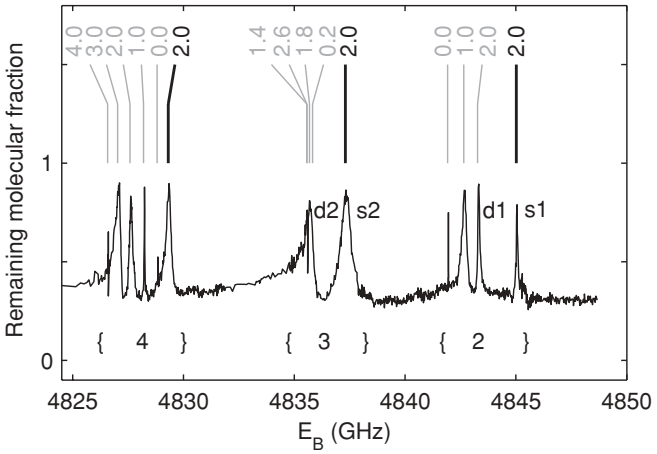

FIG. 4. Scan of the hyperfine, rotational, and Zeeman structure in the $a^3\Sigma_u^+(v = 6)$ manifold using an excited level $|e\rangle$ with 0_g^- character. The x axis shows the binding energy E_B. The quantum number f is shown below each of the three groups of lines. Thick black lines above the spectrum indicate states with $N = 0$; gray lines correspond to states with $N = 2$. The upper row of numbers indicates the expectation values of the magnetic quantum number m_f at the magnetic field of 1005.8 G.

is also a good quantum number for this lowest level in the 0_g^- manifold. Thus, when using the state with 0_g^- character, only final states $|v\rangle$ with $N = 0,2$ can be addressed in the $a^3\Sigma_u^+$ state due to the selection rule $\Delta N = \pm 1$.

The overall structure of each vibrational level can be understood with a relatively simple effective Hamiltonian [33]:

$$H = \frac{A}{2}\mathbf{S}\cdot\mathbf{I} + B_v\mathbf{N}^2 + \mu_B g_S S_z B_z,$$

with the atomic hyperfine structure constant $A = 3.42$ GHz $\times 4\pi^2/h$ [34], the total electronic and nuclear spin operator $\mathbf{S}$ and $\mathbf{I}$, respectively, and the operator for molecular rotation $\mathbf{N}$. B_v is the rotational constant of the desired vibrational level v. The last term describes the Zeeman effect of the electronic spin when exposed to an external magnetic field B_z in the z direction. The nuclear Zeeman term is neglected. The Zeeman effect can be evaluated for the case of strong hyperfine coupling such that f (with $\mathbf{f} = \mathbf{S} + \mathbf{I}$) is still a good quantum number. Using a simple vector model for $\mathbf{f}$ one can derive a Landé factor g_f:

$$\begin{aligned} H &= \frac{A}{2}\mathbf{S}\cdot\mathbf{I} + B_v\mathbf{N}^2 + \mu_B g_f m_f B_z, \\ \text{with}\quad g_f &= \frac{g_S}{2}\left(1 + \frac{S(S+1) - I(I+1)}{f(f+1)}\right). \end{aligned} \tag{1}$$

For each f, the $N = 2$ group is shifted to lower binding energy by $6B_v$ compared to $N = 0$, corresponding to about 2 GHz for the $v = 6$ manifold (see Fig. 4). Each $N = 2$ group is split by the Zeeman energy according to the m_f quantum number of each line. Only those lines which have quantum numbers where $M = 2 = m_f + m_N$ can be observed. The level $f = 3$ has a small g_f factor (1/6 for $I = 3$), which gives rise to a small Zeeman splitting. Additionally, one sees that the splitting between $f = 4$ and $f = 2$, which would be about 12 GHz for the pure hyperfine part, is enlarged by a Zeeman

contribution because of the different signs of g_f for $f = 4$ and $f = 2$. In Fig. 4 the expectation values for m_f resulting from the coupled channel model are given in the upper row and show that these lead to good quantum numbers for $f = 4$ and $f = 2$ but are less good for $f = 3$, where the hyperfine and electronic Zeeman energies are small. The mixing of states with different m_f for $f = 3$ is not included in the simple model of Eq. (1).

As discussed before, for the intermediate state with 0_g^- character we exclusively observed $N = 0$ and $N = 2$ levels in the $a^3\Sigma_u^+$ potential. This restriction does not necessarily apply when using the intermediate level $|e\rangle$ with 1_g character. The corresponding spectrum in Fig. 3(a) shows the same $v = 6$ manifold as in Fig. 4, only $|e\rangle$ has 1_g instead of 0_g^- character. It has additional lines (at ~4838 and ~4832 GHz) which match the predicted positions of $N = 4$ levels.

As mentioned in Sec. III A the level $|e\rangle$ with 1_g character would be described by a superposition of $N = 1$ and $N = 3$ states in a Hund's case (b) basis. We thus expect to see transitions to levels with $N = 0,2,4$ of the $a^3\Sigma_u^+$ state according to the selection rule $\Delta N = \pm 1$. In order to avoid confusion, we note that the $N = 0$ and $N = 2$ lines between 4825 and 4830 GHz which are clearly visible in Fig. 4 are weak or are not even observed in Fig. 3. For the same reasons as discussed at the end of Sec. II, the experimental step size of about 10 MHz might have been too large compared to the narrow linewidths for these transitions to be seen.

It was not always necessary to carry out a complete scan as in Fig. 4 in order to assign quantum numbers to observed lines in arbitrary vibrational levels. Often it was sufficient to measure a few characteristic lines and splittings and to compare them to the calculated spectrum. These data were then used to optimize the coupled channel model along with its $a^3\Sigma_u^+$ and $X^1\Sigma_g^+$ Born-Oppenheimer potentials.

IV. COUPLED-CHANNEL MODEL AND OPTIMIZATION OF THE $a^3\Sigma_u^+$ POTENTIAL

In our work we use a coupled-channel model [35–37] that can calculate all bound states of the $X^1\Sigma_g^+$ and $a^3\Sigma_u^+$ states, which correlate with the atomic asymptote $5^2S_{1/2} + 5^2S_{1/2}$. The program has helped us with the search for lines as well as with their identification. Using our data we are able to optimize the Born-Oppenheimer potential of the $a^3\Sigma_u^+$ state as well as to improve the potential of the ground state $X^1\Sigma_g^+$ given in [38]. In the following we briefly describe the model and explain how the $X^1\Sigma_g^+$ and $a^3\Sigma_u^+$ Born-Oppenheimer potentials are optimized.

To cover the full range of experimental data by a single theoretical model, only a coupled-channel analysis is adequate. It includes the calculation of the molecular bound states as well as the scattering resonances. It takes into account the $X^1\Sigma_g^+$ and $a^3\Sigma_u^+$ potential functions, the hyperfine coupling, the Zeeman interaction, rotation and the effective spin-spin interaction. Such a theoretical approach is described in several articles (e.g., [39]).

For the present analysis we include our measurements covering 135 lines of the $a^3\Sigma_u^+$ state as well as data from other work. For the $X^1\Sigma_g^+$ ground state we added data from Fourier transform spectroscopy by Seto *et al.* [38] with more than 12 000 lines. We also include measurements of Feshbach resonances for the three isotopologues $^{85}Rb_2$, $^{87}Rb_2$, and $^{85}Rb^{87}Rb$ [19–22], the four asymptotic levels from [23], and measurements from Fourier transform spectroscopy for the $a^3\Sigma_u^+$ state reported by Beser *et al.* [17].

The full Hamiltonian (cf. [39–41]) for a pair of atoms A and B can be written in the form

$$\begin{aligned} H = {} & T_n + U_X(R)P_X + U_a(R)(1 - P_X) + a_A(R)\mathbf{s}_A \cdot \mathbf{i}_A \\ & + a_B(R)\mathbf{s}_B \cdot \mathbf{i}_B + [(g_{sA}s_{zA} - g_{iA}i_{zA}) \\ & + (g_{sB}s_{zB} - g_{iB}i_{zB})]\mu_B B_z + \tfrac{2}{3}\lambda(R)\left(3S_Z^2 - S^2\right). \end{aligned} \quad (2)$$

In the present case of the homonuclear molecule $^{87}Rb_2$ the parameters with index A are equal to those of index B. The first term in the first line shows the kinetic energy T_n where we take the atomic masses from recent tables by G. Audi *et al.* [42]. The next two terms describe the potential energies U_X and U_a for the motion of the atoms, where P_X and $1 - P_X$ are projection operators on to the uncoupled states X and a, respectively. R corresponds to the internuclear separation of the two atoms. The second line shows the hyperfine interaction between the atomic electron spins $\mathbf{s}_{A,B}$ and the atomic nuclear spins $\mathbf{i}_{A,B}$. The main contribution to the functions $a_{A,B}(R)$ is the Fermi contact term. The R dependence of the hyperfine parameters accounts for several effects: It takes into account the electronic distortions of one atom by the other, that is, the binding, and an effective coupling of the electron spin of one atom with the nuclear spin of the other atom. We start with R-independent atomic coupling constants taken from a compilation by Arimondo *et al.* [43]. These constants are later refined by a simple Ansatz for the R dependence [discussed in Eq. (8)]. We neglect the nuclear quadrupole moment in the hyperfine interaction, which might come into play for deeply bound levels. The third line in Eq. (2) gives the Zeeman energy from the coupling of the electron spin and the nuclear spin with an external homogeneous magnetic field B_z in the z direction. The electronic and nuclear g factors for the atomic ground state of the Rb isotopes are taken from the report in [43]. This term couples states with different f quantum numbers. The last line contains the spin-spin interaction which couples different N states of basis (b). It is formed by the total molecular spin S and its projection on the molecule fixed axis Z. The parameter λ is a function of R, of which one part has $1/R^3$ dependence as a result from the magnetic dipole-dipole interaction. In addition, λ contains contributions from second-order spin-orbit interactions. The final analysis showed that such a contribution is significant within the achieved experimental accuracy. For example, this was important for the precise location of Feshbach resonances involving $l = 1$ and $l = 2$ levels.

The functional form of the two Born-Oppenheimer potentials, $X^1\Sigma_g^+$ and $a^3\Sigma_u^+$, is split into three regions on the internuclear separation axis R: the short-range repulsive wall ($R < R_{SR}$), the asymptotic long-range region ($R > R_{LR}$), and the intermediate deeply bound region in between. The analytic form of the potentials in the intermediate range, U_{IR}, is described by a finite power expansion of a nonlinear function ξ which depends on the internuclear separation R,

$$U_{IR}(R) = \sum_{i=0}^{n} a_i \xi^i(R), \quad (3)$$

$$\xi(R) = \frac{R - R_m}{R + bR_m}. \quad (4)$$

Here the a_i are fitting parameters (see Table II). We choose b and R_m such that only few parameters a_i are needed for describing the steep slope at the short internuclear separation side and the much smaller slope at the large R side. R_m is chosen close to the value of the equilibrium separation. The potential is extrapolated for $R < R_{SR}$ by the short-range part U_{SR} with

$$U_{SR}(R) = u_1 + u_2/R^{N_s}. \quad (5)$$

We adjust the parameters u_1 and u_2 to get a continuous transition at R_{SR}. The final fit uses $N_s \approx 4.5$ for both the $X^1\Sigma_g^+$ and $a^3\Sigma_u^+$ states.

For large internuclear distances ($R > R_{LR}$), we adopted the standard long-range form of molecular potentials,

$$U_{LR}(R) = -C_6/R^6 - C_8/R^8 - C_{10}/R^{10} \pm E_{exch}, \quad (6)$$

where the exchange contribution given by [44]

$$E_{exch} = A_{ex} R^{\gamma} \exp(-\beta R) \quad (7)$$

is negative for the singlet and positive for the triplet potential. By adjusting the parameter a_0 in Eq. (3) we can assure a continuous transition from U_{LR} to U_{IR}. As mentioned, the data on hand include three different isotopologues, namely, $^{85}Rb_2$, $^{87}Rb_2$, and $^{85}Rb^{87}Rb$. Using a model developed earlier for LiK [45] we checked in the final calculations that the data are not sufficiently precise to extract deviations from the Born-Oppenheimer approximation. Thus, we derive the potentials without any mass scaling correction.

Having discussed the complete physical model, we are now ready to calculate all the relevant bound-state energies and scattering properties to compare them with the experimental data. We have decided to evaluate the Hamiltonian in Hund's basis (e) as f is still a relatively good quantum number. This is due to the fact that the hyperfine interaction is larger than the Zeeman interaction in our experiment. As the total electron spin is not a good quantum number in Hund's case (e), the choice of this basis leads to significant nondiagonal matrix elements from the Born-Oppenheimer potentials, which are given for a pure singlet or triplet state.

We evaluate the free parameters of the model with a self-consistent iteration loop and alternate between: (i) coupled channel calculations of the full Hamiltonian and (ii) solving the Schrödinger equation separately for the states $X^1\Sigma_g^+$ and $a^3\Sigma_u^+$ using only the first line of Eq. (2) and applying the Numerov procedure. The coupled channel calculations in step (i) are used to determine the hyperfine and Zeeman structure. From this we construct hyperfine free spectroscopic data. This data is the input for the Born-Oppenheimer potential fits in step (ii). We incorporate the fitting routine for the plain Born-Oppenheimer potentials in step (ii). The optimization of the singlet and triplet potentials is done simultaneously as both potentials have a common asymptote. These asymptotic potentials are given in Eq. (6) with equal dispersion coefficients.

Normally, the iteration loop between the potential function fit and the coupled channel calculation for producing hyperfine structure free data converges in a few steps, but we observed some systematic deviations between measurements and calculations. Specifically, the hyperfine splitting showed variations of a few percent within the vibrational ladder. Even though our experimental accuracy is not better than 30 MHz, such small variations are observable since the hyperfine splitting in $^{87}Rb_2$ of 12 GHz is so large.

In order to theoretically account for the hyperfine variations, we extended the model. We changed the fixed atomic hyperfine parameters to a function in R. We chose a function which switches at a distance R_0 from the atomic value of the hyperfine constant to another value for a deeply bound dimer,

$$a_{A/B} = a_{Rb}\left(1 + \frac{c_f}{e^{(R-R_0)/\Delta R} + 1}\right). \quad (8)$$

Here a_{Rb} is the atomic hyperfine constant, c_f the fractional change of the constant, and R_0 and ΔR describe the switching distance and its width, respectively. We also tried several other simple switching functions, which produced about equal fit quality. The function in Eq. (8) is easily applicable for other isotopes by introducing the proper atomic hyperfine constant, because the scaling c_f will be independent of the isotope. We chose $R_0 = 11.0a_0$ and $\Delta R = 0.5a_0$ (where $a_0 = 0.5292 \times 10^{-10}$ m is the Bohr radius), such that switching takes place approximately at the minimum of the $a^3\Sigma_u^+$ potential. From our fits we obtained an amplitude $c_f = -0.0778$, which corresponds to a variation of the hyperfine coupling across the potential depth of up to 8%. The influence of this hyperfine variation within an individual vibrational manifold will be smaller because of the averaging of Eq. (8) over the vibrational wave function. As mentioned before, also the spin-spin interaction needs optimization in order to explain systematic shifts of Feshbach resonances in s-wave and p-wave scattering channels, as measured in [19]. The spin-spin interaction couples different partial waves l subject to the selection rule $\Delta l = 0, \pm 2$ such that resonances in a s-wave scattering channel involve bound states with $l = 0$ and $l = 2$. In higher order this also involves states with $l = 4$ etc. The spin-spin interaction splits the resonances according to $|m_l|$, the projection quantum number of rotation on the space fixed axis. We use a simple functional form for $\lambda(R)$ in Eq. (2),

$$\lambda(R) = -\frac{3}{4}\alpha^2\left(\frac{1}{R^3} + a_{SO}\exp\left[-b(R - R_{SO})\right]\right), \quad (9)$$

that consists of two terms. The first term represents the magnetic dipole-dipole interaction and the second term is the second-order spin-orbit contribution. If Eq. (9) is given in atomic units, α is the fine structure constant. Since the few data at hand cannot be highly sensitive to the actual function, we adopted values for b and R_{SO} from a theoretical approach by Mies *et al.* for Rb_2 [46] ($b = 0.7196a_0^{-1}$ and $R_{SO} = 7.5a_0$). We fitted the parameter a_{SO}, which yielded $a_{SO} = -0.0416a_0^{-3}$. With these parameters the second part in Eq. (9) contributes significantly to the effective spin-spin interaction in the internuclear separation interval $R < 20a_0$. This affects bound levels of the triplet state that determine the Feshbach resonances. After optimization we achieve an accuracy of 0.1 G. This correction to the constant λ does not influence the description of the other bound states within their uncertainty.

Finally, we found that we can improve the fit by adding to the long range formula Eq. (6) a term of the form $-C_{26}/R^{26}$ with an amplitude C_{26}, which contributes about a thousandth of the total long-range energy at the connection point $R_{\rm LR}$. The exponent of 26 was chosen so that the term is negligible outside a small region around the long-range connection point $R = R_{\rm LR}$.

The final parameter sets of the potentials are shown in Tables I and II for the singlet and triplet states, respectively. The derived potentials and the corrections defined previously agree very closely with all observations to within their experimental uncertainties, and the normalized standard deviation (i.e., standard deviation divided by experimental uncertainty) is close to one. In fact, depending on which of our experimental data sets (hyperfine free spectra, binding energies from dark-state spectroscopy or Feshbach resonances) we compare to the model calculations, the normalized standard deviations only vary slightly, ranging from 1.01 to 1.3. The normalized standard deviation from the joint calculation over the huge body of rovibrational energies (12 459 data points from the states $X^1\Sigma_g^+$ and $a^3\Sigma_u^+$) is about 1.01, which is quite satisfactory.

As another result of our analysis, we were able to eliminate an ambiguity in the rotational assignment of the Fourier transform spectroscopy data reported by Beser *et al.* for the state $a^3\Sigma_u^+$ [17]. The authors stated in the rotational assignment an ambiguity by $\Delta N = \pm 1$. We determined that the shift of the rotational quantum number must be $\Delta N = +1$. Afterward, we used the data from [17] with that assignment for the further fits. The result in Table II includes these data

TABLE I. Parameters of the analytic representation of the potential of state $X^1\Sigma_g^+$. The energy reference is the dissociation asymptote and the term energy T_e^X is the depth of the potential. Parameters with $*$ are set for continuous extrapolation of the potential; for those with $**$, see text for interpretation.

	$R < R_{\rm SR} = 3.126$ Å
N_s	4.533 89
u_1^*	$-0.638\,904\,880 \times 10^4$ cm^{-1}
u_2^*	$0.112\,005\,361 \times 10^7$ cm^{-1} Å^{N_s}
	$R_{\rm SR} \leqslant R \leqslant R_{\rm LR} = 11.000$ Å
b	−0.13
$R_{\rm m}$	4.209 912 760 Å
a_0	−3993.592 873 cm^{-1}
a_1	0.000 000 000 000 000 000 cm^{-1}
a_2	$0.282\,069\,372\,972\,346\,137 \times 10^5$ cm^{-1}
a_3	$0.560\,425\,000\,209\,256\,905 \times 10^4$ cm^{-1}
a_4	$-0.423\,962\,138\,510\,562\,945 \times 10^5$ cm^{-1}
a_5	$-0.598\,558\,066\,508\,841\,584 \times 10^5$ cm^{-1}
a_6	$-0.162\,613\,532\,034\,769\,596 \times 10^5$ cm^{-1}
a_7	$-0.405\,142\,102\,246\,254\,944 \times 10^5$ cm^{-1}
a_8	$0.195\,237\,415\,352\,729\,586 \times 10^6$ cm^{-1}
a_9	$0.413\,823\,663\,033\,582\,852 \times 10^6$ cm^{-1}
a_{10}	$-0.425\,543\,284\,828\,921\,501 \times 10^7$ cm^{-1}
a_{11}	$0.546\,674\,790\,157\,210\,198 \times 10^6$ cm^{-1}
a_{12}	$0.663\,194\,778\,861\,331\,940 \times 10^8$ cm^{-1}
a_{13}	$-0.558\,341\,849\,704\,095\,051 \times 10^8$ cm^{-1}
a_{14}	$-0.573\,987\,344\,918\,535\,471 \times 10^9$ cm^{-1}
a_{15}	$0.102\,010\,964\,189\,156\,187 \times 10^{10}$ cm^{-1}
a_{16}	$0.300\,040\,150\,506\,311\,035 \times 10^{10}$ cm^{-1}
a_{17}	$-0.893\,187\,252\,759\,830\,856 \times 10^{10}$ cm^{-1}
a_{18}	$-0.736\,002\,541\,483\,347\,511 \times 10^{10}$ cm^{-1}
a_{19}	$0.423\,130\,460\,980\,355\,225 \times 10^{11}$ cm^{-1}
a_{20}	$-0.786\,351\,477\,693\,491\,840 \times 10^{10}$ cm^{-1}
a_{21}	$-0.102\,470\,557\,344\,862\,152 \times 10^{12}$ cm^{-1}
a_{22}	$0.895\,155\,811\,349\,267\,578 \times 10^{11}$ cm^{-1}
a_{23}	$0.830\,355\,322\,355\,692\,902 \times 10^{11}$ cm^{-1}
a_{24}	$-0.150\,102\,297\,761\,234\,375 \times 10^{12}$ cm^{-1}
a_{25}	$0.586\,778\,574\,293\,387\,070 \times 10^{11}$ cm^{-1}
	$R > R_{\rm LR}$
C_6	$0.227\,003\,2 \times 10^8$ cm^{-1} Å^6
C_8	$0.778\,288\,6 \times 10^9$ cm^{-1} Å^8
C_{10}	$0.286\,886\,9 \times 10^{11}$ cm^{-1} Å^{10}
C_{26}^{**}	$0.281\,981\,0 \times 10^{26}$ cm^{-1} Å^{26}
$A_{\rm ex}$	$0.131\,778\,6 \times 10^5$ cm^{-1} Å$^{-\gamma}$
γ	5.317 689
β	2.093 816 Å^{-1}
	Derived constants
Equilibrium distance	$R_e^X = 4.209\,91(5)$ Å
Electronic term energy	$T_e^X = -3993.592\,8(30)$ cm^{-1}

TABLE II. Parameters of the analytic representation of the potential of state $a^3\Sigma_u^+$. The energy reference is the dissociation asymptote and the term energy T_e^a is the depth of the potential. Parameters with $*$ are set for continuous extrapolation of the potential; for those with $**$, see text for interpretation.

	$R < R_{\rm SR} = 5.07$ Å
N_s	4.533 895 0
u_1^*	$-0.619\,088\,543 \times 10^3$ cm^{-1}
u_2^*	$0.956\,231\,677 \times 10^6$ cm^{-1} Å^{N_s}
	$R_{\rm SR} \leqslant R \leqslant R_{\rm LR} = 11.00$ Å
b	−0.33
$R_{\rm m}$	6.093 345 1 Å
a_0	−241.503 352 cm^{-1}
a_1	−0.672 503 402 304 666 542 cm^{-1}
a_2	$0.195\,494\,577\,140\,503\,543 \times 10^4$ cm^{-1}
a_3	$-0.141\,544\,168\,453\,406\,223 \times 10^4$ cm^{-1}
a_4	$-0.221\,166\,468\,149\,940\,465 \times 10^4$ cm^{-1}
a_5	$0.165\,443\,726\,445\,793\,004 \times 10^4$ cm^{-1}
a_6	$-0.596\,412\,188\,910\,614\,259 \times 10^4$ cm^{-1}
a_7	$0.654\,481\,694\,231\,538\,040 \times 10^4$ cm^{-1}
a_8	$0.261\,413\,416\,681\,972\,012 \times 10^5$ cm^{-1}
a_9	$-0.349\,701\,859\,112\,702\,878 \times 10^5$ cm^{-1}
a_{10}	$-0.328\,185\,277\,155\,018\,630 \times 10^5$ cm^{-1}
a_{11}	$0.790\,208\,849\,885\,562\,522 \times 10^5$ cm^{-1}
a_{12}	$-0.398\,783\,520\,249\,289\,213 \times 10^5$ cm^{-1}
	$R > R_{\rm LR}$
C_6	$0.227\,003\,2 \times 10^8$ cm^{-1} Å^6
C_8	$0.778\,288\,6 \times 10^9$ cm^{-1} Å^8
C_{10}	$0.286\,886\,9 \times 10^{11}$ cm^{-1} Å^{10}
C_{26}^{**}	$0.281\,981\,0 \times 10^{26}$ cm^{-1} Å^{26}
A_{ex}	$0.131\,778\,6 \times 10^5$ cm^{-1} Å$^{-\gamma}$
γ	5.317 689
β	2.093 816 Å^{-1}
	Derived constants
Equilibrium distance	$R_e^a = 6.094\,0(10)$ Å
Electronic term energy	$T_e^a = -241.503\,4(30)$ cm^{-1}

and will give a better confidence in predicting rotational levels with higher rotational quantum numbers.

V. PROGRESSION OF VIBRATIONAL LEVELS AND THEIR SUBSTRUCTURE

In the following we discuss interesting insights which we have gained from our analysis of the coupled system. In particular, we investigate the progression of several quantities in the vibrational ladder and the mixing of singlet and triplet states. We concentrate on the details of the $a^3\Sigma_u^+$ state because it was studied in full resolution of hyperfine and Zeeman energy over the whole vibrational ladder. Such a body of data does not exist for any other alkali-metal dimer.

A. Vibrational ladder and rotational progression

We return to the vibrational states shown in Fig. 2, which allows us to compare in detail the optimized coupled-channel model with our experimental findings for all vibrational states.

The binding energies given in Fig. 2(a) correspond to the most deeply bound level in each vibrational level, that is, the state with quantum numbers $N = 0$, $f = 2$ (at 0 G) and $M = 2$. We will refer to this level as "s1". The s1 level of $v = 0$ in the $a^3\Sigma_u^+$ potential is also the lowest bound state in that potential and has an observed binding energy of (7038.067 ± 0.050) GHz $\times h$ at 1005.8 G with respect to the lowest atomic asymptote $f_A \approx 1$, $m_A = 1$ and $f_B \approx 1$, $m_B = 1$. A list of all the other measured and calculated bound-state energies together with their expectation values of the quantum numbers can be found in the supplementary material [47].

Figure 2(b) shows the residues between our experimental s1 data and the optimized model. In general, the model agrees very well with the measurements to within the error bars. The data points with larger error bars belong to early measurements without simultaneous wave-meter reading of both lasers, which leads to a significant increase in the experimental uncertainty (see Sec. II).

We now investigate the progression of the rotational splitting in the vibrational ladder. For this, we consider the s1 level ($N = 0$) and its nearest neighbor in our spectra with ($N = 2$) which we call "d1" (see Figs. 3 and 4). The s1 and d1 levels both have $f = 2$ and $m_f = 2$. Thus, the splitting between them is to a high degree rotational energy. The splitting decreases with increasing v, which is due to the fact, that the mean distance between the Rb_2 nuclei (and hence the effective moment of inertia) increases as v increases. We have directly observed this behavior in our experiments (see Fig. 5). There is very good agreement between the experimental data and the calculation (continuous line) using the optimized potential of the $a^3\Sigma_u^+$ state.

Besides the s1 level ($N = 0, f = 2$) and the d1 level ($N = 2, f = 2$) we also observe states with $N = 4$ and $f = 2$ for several low lying vibrational levels. The two lines in Fig. 3(a) at 4839 GHz and the two lines in Fig. 3(b) at 7032 GHz have $N = 4$. Observation of these levels improved the precision when fixing the position of the $a^3\Sigma_u^+$ potential minimum in terms of the internuclear distance, or the effective rotational constant B_v. This turned out to be important for the reassignment of the observations by Beser *et al.* [17], as discussed at the end of Sec. IV.

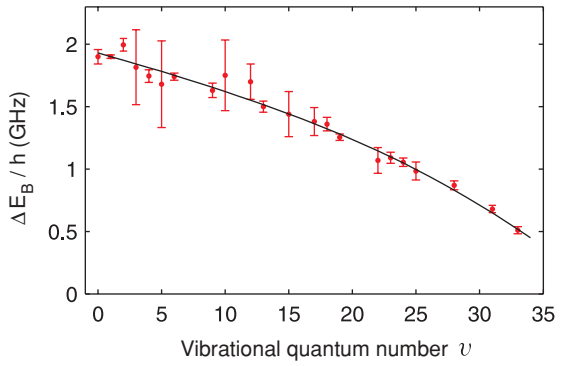

FIG. 5. (Color online) Energy splitting ΔE_B between the s1 level ($N = 0$) and the d1 level ($N = 2$) for a given vibrational quantum number v. Large error bars correspond to early measurements without simultaneous wave-meter readings (see text). The continuous line is a calculation based on the coupled-channel model.

B. Hyperfine splitting and singlet-triplet mixing

It is instructive to investigate the progression of the multiplet structure of the vibrational levels. Figure 6(a) shows calculated levels for $M = 2$ stacked on top of each other for increasing v of the $a^3\Sigma_u^+$ potential. We concentrate on the triplet states ($S = 1$) with rotation $N = 0,2$ and we restrict ourselves further to triplet levels with $I = 3$. Additionally, we show singlet levels ($S = 0$) with $I = 2$ that are located in the vicinity of the triplet levels. Thus, the typical stick spectrum of each vibrational manifold in the $a^3\Sigma_u^+$ state looks like the one in Fig. 4. There are three groups of lines with $f = 4,3,2$, respectively. The vibrational quantum number v runs from 0 to 34, where the multiplets do not yet overlap for different vibrational levels.

In order to properly stack the data, we have chosen the level with $N = 0$, $f \approx 3$ to be the energy reference ($\Delta E_B = 0$) for each vibrational level. We call this level "s2" (see also Figs. 3 and 4). This level is quite insensitive to mixing with singlet levels, which makes it a good reference because there is no singlet level with $f = 3$ and even parity for direct coupling. It is clear from Fig. 6(a), that the multiplet structure of different vibrational manifolds is similar, at least from $v = 0$ to about $v = 30$, as expected from the simple model Hamiltonian in Eq. (1). The structure changes in a smooth and monotonical way with v. For each of the quantum numbers $f = 4,3,2$ the splitting between $N = 0$ and $N = 2$ decreases with increasing v as discussed in Sec. V A.

Appreciable mixing of a singlet and a triplet level can occur when the two levels with $f = 2$ are located energetically closely enough, in our case within a few GHz, corresponding to the strength of the hyperfine interaction. One effect of mixing is a shift of the level positions due to level repulsion, clearly seen in Fig. 6. For $v = 24$, for example, the triplet lines of $f = 2$ are pushed to the left by about 0.4 GHz by the close singlet levels on the right-hand side. For $v < 20$ we also observe narrow coincidences between triplet and singlet levels, for example, for $v = 15$. Here almost no perturbation appears in the graph, in contrast to the case $v = 24$. We attribute this to

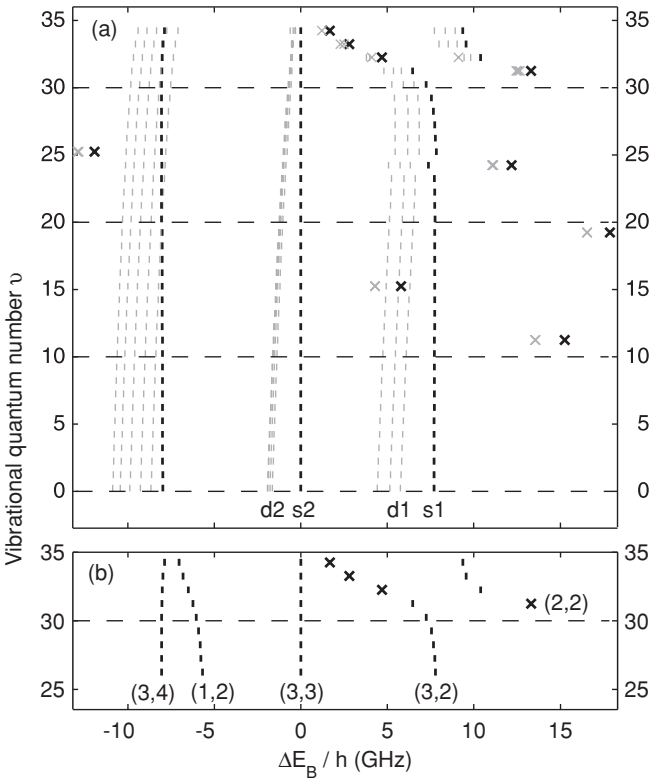

FIG. 6. (a) Progression of the substructure of the vibrational manifold at $B = 1005.8$ G. Shown are calculated $a^3\Sigma_u^+$ levels with quantum numbers $I \approx 3$, $M = 2$, $N = 0,2$, and $v = 0 \cdots 34$. Thick black lines correspond to $N = 0$, gray ones to $N = 2$. The s2 level serves as energy reference ($\Delta E_B = 0$) in each vibrational substructure. In addition to the triplet levels, nearby singlet levels of the $X^1\Sigma_g^+$ potential are also shown (thick black crosses, $N = 0$; gray crosses, $N = 2$). (b) Symbols as in panel (a). To discuss the singlet-triplet mixing from a theoretical point of view, we now also include lines with $I \approx 1$ but only $N = 0$ for clarity. On the bottom, the approximate quantum numbers (I, f) are given. See text for details.

a significantly lower overlap of the vibrational wave functions of the singlet and triplet levels for the case $v = 15$ compared to that of $v = 24$. For vibrational quantum numbers $v > 30$ mixing is very strong and happens for every vibrational level. Because the long-range behavior of the $a^3\Sigma_u^+$ and $X^1\Sigma_g^+$ states is similar, the overlap of the wave functions will become large for high v. The vibrational spacing will become similar to the hyperfine splitting, and the state vectors here are best described by Hund's coupling case (e), that is, quantum numbers of atom pairs.

Singlet-triplet mixing not only occurs for triplet molecules with $I = 3$ but also for $I = 1$. Figure 6(b) shows ($N = 0$) triplet levels with $I = 3$ and $I = 1$ for $v = 25$ to 34. The repulsion of the $I = 1$ levels from the singlet levels is clearly visible. The figure shows an avoided-crossing-like behavior for the levels on the right as a function of v, indicating the strong mixing between $I = 3$ and $I = 2$, which also means that u-g symmetry is broken for these levels. Further, our calculations show that only levels with the same f and N quantum numbers mix considerably. The singlet lines shown here have $f = 2$ and $N = 0$. Apparently, despite the relatively strong magnetic

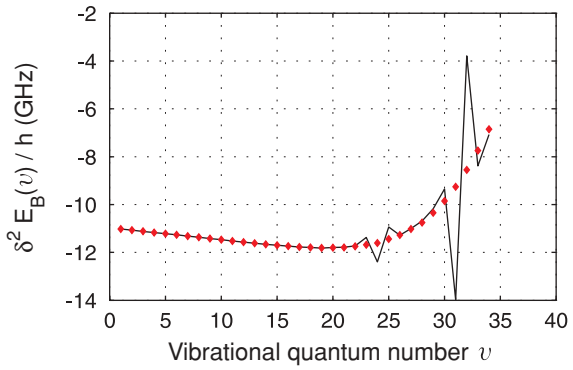

FIG. 7. (Color online) "Discrete second derivative" of $E_B(v)$, that is, $\delta^2 E_B(v) = E_B(v+1) - 2E_B(v) + E_B(v-1)$. The solid curve connects the points from the s1 levels, while the diamonds correspond to the s2 state.

fields of about 1000 G f is still quite a good quantum number. Indeed, f appears as quantum number in both state vectors for Hund's case (b) and (e) and loses its meaning only for much higher magnetic fields. N is good due to the small effective spin-spin interaction.

The shift in position due to mixing can be traced more clearly with a simple difference method discussed in the following. Figure 7 shows the "discrete second derivative" $\delta^2 E_B(v)$ of the function for the binding energies $E_B(v)$, that is, $\delta^2 E_B(v) = E_B(v+1) - 2E_B(v) + E_B(v-1)$. In other words, it is the difference between the neighboring energy splittings. The curve calculated from binding energies s1 exhibits sudden jumps for particular vibrational levels. These are due to singlet-triplet mixing and the v positions are consistent with Fig. 6. In contrast, the $\delta^2 E_B(v)$ curve for the s2 state is smooth, and thus does not indicate mixing with the singlet lines, which justifies its choice as energy reference in Fig. 6.

We have confirmed the singlet-triplet mixing experimentally. Figure 8 shows scans of parts of the vibrational levels $v = 28,31,33$, where the intermediate level $|e\rangle$ with 1_g character was used (see also Fig. 3). The s2 level is chosen to be the energy reference at $\Delta E_B = 0$ as before. For $v = 28$ we observe a line structure similar to that of Figs. 3 and 4. Thus, we take the $v = 28$ spectrum as reference of the pure case "triplet." In fact, from our calculations we see that the next singlet level is located about 30 GHz away. This detuning gives rise to only a very small mixing which slightly lowers the triplet character of the s1 level to 0.99. The singlet level obtains a triplet character of 0.02. However, due to the selection rule $\Delta S = 0$, the transition to the intermediate state $|e\rangle$ with its very pure triplet character would simply be too weak to see.

This situation changes drastically for $v = 31$ and 33. Two additional lines are visible in the spectrum which originate from singlet states with $M = 2$, $N = 0$ and 2 . Here the singlet-triplet mixing is close to 40%, which makes the singlet lines easily detectable. Additionally, for $v = 31$ the s1 and d1 components are shifted to lower values than expected from the reference spectrum $v = 28$ due to repulsion by the singlet component on the high energy side. In the case of $v = 33$ the singlet component pushes the s1 and d1 in the opposite direction. Our calculations show that even the chosen energy reference s2 starts to show mixing, indicated by its reduced

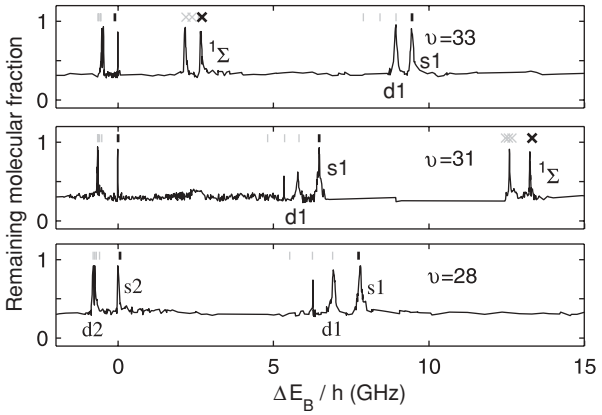

FIG. 8. Observation of strongly perturbed singlet levels. We compare sections of line spectra for the vibrational levels $v = 28$, 31, and 33. As in Fig. 6 the s2 level is chosen as energy reference $\Delta E_B = 0$. The lines (and crosses) above the experimentally observed spectrum are from coupled-channel calculations. Black lines (crosses) represent $N = 0$ levels, while thin gray lines (crosses) correspond to $N = 2$ levels for $S = 1$ ($S = 0$, respectively). The lines that originate from the singlet states are labeled with "$^1\Sigma$".

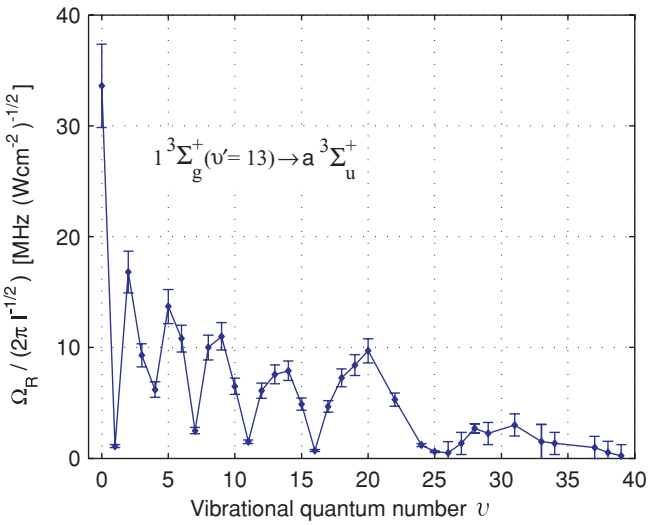

FIG. 9. (Color online) Normalized transition matrix element $\Omega_2/(2\pi\sqrt{I_2})$ between the excited level $|e\rangle$ ($v' = 13, 1_g$ character) in the $1^3\Sigma_g^+$ potential and the s1 level with vibrational quantum number v in the lowest triplet potential $a^3\Sigma_u^+$.

triplet character of 0.98. In parallel to the singlet-triplet mixing, the quantum number I loses its meaning as well; for example, the level s1 of $v = 33$ has an expectation value for I of 2.75 instead of 3, due to a significant contribution of $I = 2$ from the singlet state. Comparing the stick spectrum line positions with observed lines in Fig. 8, we note the very nice agreement between experiment and theory. We want to mention that we measured the singlet levels at the predicted positions from first calculations. This emphasizes the predictive power of the presented model.

The fact that we observe singlet-triplet mixing for relatively deeply bound levels with binding energies of a few hundred GHz $\times$ h is already quite interesting. In addition, it provides valuable information for fixing the energy position of the triplet levels with respect to the singlets with high precision. This is especially important for the large body of data of the singlet system (see Sec. IV), which was obtained with no connection to the triplet state [38].

C. Franck-Condon overlap

When scanning over all vibrational levels, the transition matrix elements for the transition from $|e\rangle$ to $|v\rangle$ are not constant but oscillate as a function of v. This oscillation is mainly due to variations in the Franck-Condon overlap between the $|e\rangle$, $v' = 13$ vibrational wave function and the vibrational wave functions $|v\rangle$ of the $a^3\Sigma_u^+$ potential. Figure 9 shows the normalized transition matrix element, $c_2 = \Omega_2(v)/(2\pi\sqrt{I_2})$, where Ω_2 is the Rabi frequency and I_2 is the intensity of laser 2. Ω_2 is determined from the measured width of the dark resonance [48,49]. For these measurements we used the excited level 1_g as $|e\rangle$ and the s1 levels as $|v\rangle$ of the $a^3\Sigma_u^+$ state. The transition matrix element c_2 varies from about (0.2–33) MHz/$\sqrt{\text{Wcm}^{-2}}$. In terms of a dipole moment, $\langle er\rangle = \Omega_2(v)/\sqrt{I_2}\hbar\sqrt{\epsilon_0 c/2}$, this corresponds to (0.05–8.0) $\times$ 10^{-30} Cm.

In comparison, the amplitude for the transition between $|i\rangle$ and $|e\rangle$ is $\Omega_1/\sqrt{I_1} = 0.4$ MHz/$\sqrt{\text{W cm}^{-2}}$. We determine Ω_1 from resonant excitation, measuring how quickly $|i\rangle$ molecules are lost for a given laser intensity I_1. The data in Fig. 9 can be used to fix the position of the $1^3\Sigma_g^+$ potential relative to the $a^3\Sigma_u^+$ potential applying the Franck-Condon approximation.

VI. CONCLUSION AND OUTLOOK

In this article we demonstrate high-resolution dark-state spectroscopy of ultracold $^{87}Rb_2$ molecules. We are able to resolve the vibrational, rotational, hyperfine, and Zeeman structure of the lowest $a^3\Sigma_u^+$ potential with an absolute accuracy as high as 30 MHz. We find that the hyperfine structure is weakly dependent on the vibrational level, which also influences predictions of Feshbach resonances if one would like to reach accuracies on the order of 0.1 G.

By optimizing mainly the triplet Born-Oppenheimer potential we obtain a model that can quite accurately predict all vibrational levels in the $a^3\Sigma_u^+$ and $X^1\Sigma_g^+$ potentials for different ranges of rotational quantum numbers. After reassigning recent data from Fourier transform spectroscopy [17], we extend the range of applicability to rotational states as high as $N = 70$ for the $a^3\Sigma_u^+$ potential. Because of this reassignment also the molecular parameters like the equilibrium internuclear separation R_e or the dissociation energy D_e have changed significantly compared to values reported in [17]. The new values are given in Table II. For rotational levels with $N \leqslant 4$ the model calculations for triplet levels of any vibrational level should have a precision similar to that of our measurements, that is, about 30 MHz. For higher N this precision will increasingly degrade resulting from the reduced accuracy of the data from [17] of about 300 MHz for $N = 70$. Compared to [38], the potential of the ground-state $X^1\Sigma_g^+$ is significantly improved close to the atomic asymptote by including data on the mixed singlet-triplet levels of this study and data on Feshbach resonances from various other sources.

We recommend the derived potential function for further use. It can predict the deeply bound levels with an accuracy (about 50 MHz), comparable to that of the Fourier transform spectroscopy in [38]. The asymptotic levels are accurate on the order of a few MHz or better as their position is determined by the precisely measured location of Feshbach resonances. We improved the description of the large set of ^{87}Rb Feshbach resonances as compared to Ref. [19] where the original calculation was based only on a few selected resonances and a derived asymptotic form of the two potentials. In [19] deviations as high as 2 G appeared and, for example, the resonances of asymptote $f_A = 1, m_A = 0 + f_B = 1, m_B = 1$ were all calculated systematically too high. In the present model these discrepancies disappear. The average deviation over all 46 resonances, given in [19–22], is about 0.15 G [50]. If one removes the R-dependence of the hyperfine coupling as given in Eq. (8), deviations in the order of 0.5 G appear varying according to the different f levels which correlate to the Feshbach resonances. To improve the overall fit, one probably might be forced to include many-body effects of the collision process for detecting the resonances. The overall improvement of the long-range behavior also allows the whole set of scattering lengths for the three isotopologues to be calculated. Table III gives a selection of these calculations. The error of these data will be in the last digit shown. These values are consistent with earlier publications but more precise and, in general, internally consistent between the isotopologues.

Our model will be valuable for our planned collision experiments of ultracold molecules which have to be prepared in well-defined quantum states. The singlet-triplet mixing that we observe is of interest for a proposed precision experiment to measure the time dependence of the electron to proton mass ratio [11] (see also [9,10]). The precision of future measurements would be mainly limited by the accuracy of the wave meter and could be improved by one or two orders of magnitude. Such a high precision could be used, for example, to test the fundamental limits of the coupled-channel model, where we assume the validity of (i) the Born-Oppenheimer approximation, (ii) using Zeeman terms with atomic parameters only, (iii) a limited functional dependence in R of the hyperfine and spin-spin interaction, and (iv) neglecting quadrupole hyperfine coupling.

TABLE III. Scattering lengths (in Bohr radius, $a_0 = 0.5292 \times 10^{-10}$ m). a_{lowest} gives the scattering length of the energetically lowest hyperfine state.

Isotope	a_{singlet}	a_{triplet}	a_{lowest}	Rb + Rb $(f,m_f) + (f,m_f)$
87/87	90.35	99.04	100.36	(1,1) + (1,1)
85/85	2720	−386.9	−460.1	(2,2) + (2,2)
87/85	11.37	201.0	229.4	(1,1) + (2,2)

ACKNOWLEDGMENTS

We thank Marius Lysebo and Leif Veseth for model calculations to characterize the excited states $|e\rangle$. We thank Matthias Gerster for studying the simple Hamiltonian in Eq. (1). We acknowledge helpful predictions from Christiane Koch on the Franck-Condon overlap for the $|e\rangle$–$|v\rangle$ transition. This work was supported by the Austrian Science Fund (FWF) within SFB 15 (Project Part 17). E.T. thanks the cluster of excellence "QUEST" for support and the Minister of Science and Culture for providing a Niedersachsenprofessur.

[1] J. G. Danzl, E. Haller, M. Gustavsson, M. J. Mark, R. Hart, N. Bouloufa, O. Dulieu, H. Ritsch, and H.-C. Nägerl, Science **321**, 1062 (2008).
[2] F. Lang, K. Winkler, C. Strauss, R. Grimm, and J. Hecker Denschlag, Phys. Rev. Lett. **101**, 133005 (2008).
[3] K.-K. Ni, S. Ospelkaus, M. H. G. de Miranda, A. Pe'er, B. Neyenhuis, J. J. Zirbel, S. Kotochigova, P. S. Julienne, D. S. Jin, and J. Ye, Science **322**, 231 (2008).
[4] M. Viteau, A. Chotia, M. Allegrini, N. Bouloufa, O. Dulieu, D. Comparat, and P. Pillet, Science **321**, 232 (2008).
[5] J. Deiglmayr, A. Grochola, M. Repp, K. Mörtlbauer, C. Glück, J. Lange, O. Dulieu, R. Wester, and M. Weidemüller, Phys. Rev. Lett. **101**, 133004 (2008).
[6] P. Staanum, S. D. Kraft, J. Lange, R. Wester, and M. Weidemüller, Phys. Rev. Lett. **96**, 023201 (2006).
[7] R. V. Krems, Int. Rev. Phys. Chem. **24**, 99 (2005).
[8] R. V. Krems, Phys. Chem. Chem. Phys. **10**, 4079 (2008).
[9] C. Chin, V. V. Flambaum, and M. G. Kozlov, New J. Phys. **11**, 055048 (2009).
[10] T. Zelevinsky, S. Kotochigova, and J. Ye, Phys. Rev. Lett. **100**, 043201 (2008).
[11] D. DeMille, S. Sainis, J. Sage, T. Bergeman, S. Kotochigova, and E. Tiesinga, Phys. Rev. Lett. **100**, 043202 (2008).
[12] K. M. Jones, E. Tiesinga, P. D. Lett, and P. S. Julienne, Rev. Mod. Phys. **78**, 483 (2006).
[13] T. Köhler, K. Goral, and P. S. Julienne, Rev. Mod. Phys. **78**, 1311 (2006).
[14] J. Weiner, V. S. Bagnato, S. Zilio, and P. S. Julienne, Rev. Mod. Phys. **71**, 1 (1999).
[15] L. E. E. de Araujo, J. D. Weinstein, S. D. Gensemer, F. K. Fatemi, K. M. Jones, P. D. Lett, and E. Tiesinga, J. Chem. Phys. **119**, 2062 (2003).
[16] J. Lozeille *et al.*, Eur. Phys. J. D **39**, 261 (2006).
[17] B. Beser, V. B. Sovkov, J. Bai, E. H. Ahmed, C. C. Tsai, F. Xie, L. Li, V. S. Ivanov, and A. M. Lyyra, J. Chem. Phys. **131**, 094505 (2009).
[18] M. Mudrich, Ph. Heister, T. Hippler, Ch. Giese, O. Dulieu, and F. Stienkemeier, Phys. Rev. A **80**, 042512 (2009).
[19] A. Marte, T. Volz, J. Schuster, S. Dürr, G. Rempe, E. G. M. van Kempen, and B. J. Verhaar, Phys. Rev. Lett. **89**, 283202 (2002).
[20] S. B. Papp and C. E. Wieman, Phys. Rev. Lett. **97**, 180404 (2006).
[21] J. L. Roberts, J. P. Burke, N. R. Claussen, S. L. Cornish, E. A. Donley, and C. E. Wieman, Phys. Rev. A **64**, 024702 (2001).
[22] M. Erhard, H. Schmaljohann, J. Kronjäger, K. Bongs, and K. Sengstock, Phys. Rev. A **70**, 031602 (2004).

[23] R. Wynar *et al.*, Science **287**, 1016 (2000).
[24] T. Volz, S. Dürr, S. Ernst, A. Marte, and G. Rempe, Phys. Rev. A **68**, 010702 (2003).
[25] G. Thalhammer, K. Winkler, F. Lang, S. Schmid, R. Grimm, and J. Hecker Denschlag, Phys. Rev. Lett. **96**, 050402 (2006).
[26] F. Lang, C. Strauss, K. Winkler, T. Takekoshi, R. Grimm, and J. Hecker Denschlag, Faraday Discuss. **142**, 271 (2009).
[27] F. Lang, Ph.D. thesis, Institut für Experimentalphysik, Universität Innsbruck, 2009.
[28] The width of the dark resonance scales as Ω_2 if laser 2 is fixed on resonance and laser 1 is scanned.
[29] B. W. Shore, *The Theory of Coherent Atomic Excitation* (Wiley, New York, 1990), Sec. 10.4.
[30] In general, we define expectation values for the quantum numbers of an operator as $\sum_i \lambda_i |\langle e_i|\Psi\rangle^2|$, where λ_i are the eigenvalues of the operator, e_i are corresponding normalized basis vectors, and $|\Psi\rangle$ is the state.
[31] C. H. Townes and A. L. Schawlow, *Microwave Spectroscopy* (McGraw-Hill, New York, 1955).
[32] G. Herzberg, *Molecular Spectra and Molecular Structure* (Van Nostrand, New York, 1950), Vol. I.
[33] T. M. Dunn, in *Molecular Spectroscopy: Modern Research*, edited by K. N. Rao and C. W. Mathews (Academic Press, San Diego, 1972), p. 231.
[34] S. Bize, Y. Sortais, M. S. Santos, C. Mandache, A. Clairon, and C. Salomon, Europhys. Lett. **45**, 558 (1999).
[35] O. Dulieu and P. S. Julienne, J. Chem. Phys. **103**, 60 (1995).
[36] E. Tiesinga, C. J. Williams, and P. S. Julienne, Phys. Rev. A **57**, 4257 (1998).
[37] M. Krauss and W. J. Stevens, J. Chem. Phys. **93**, 4236 (1990).
[38] J. Y. Seto, R. J. LeRoy, J. Vergès, and C. Amiot, J. Chem. Phys. **113**, 3067 (2000).
[39] A. Pashov, O. Docenko, M. Tamanis, R. Ferber, H. Knöckel, and E. Tiemann, Phys. Rev. A **76**, 022511 (2007).
[40] F. H. Mies and M. Raoult, Phys. Rev. A **62**, 012708 (2000).
[41] T. Laue, E. Tiesinga, C. Samuelis, H. Knöckel, and E. Tiemann, Phys. Rev. A **65**, 023412 (2002).
[42] G. Audi, A. H. Wapstra, and C. Thibault, Nucl. Phys. **729**, 337 (2003).
[43] E. Arimondo, M. Inguscio, and P. Violini, Rev. Mod. Phys. **49**, 31 (1977).
[44] B. M. Smirnov and M. S. Chibisov, Zh. Eksp. Teor. Fiz. **48**, 939 (1965) [Sov. Phys. JETP **21**, 624 (1965)].
[45] E. Tiemann, H. Knöckel, P. Kowalczyk, W. Jastrzebski, A. Pashov, H. Salami, and A. J. Ross, Phys. Rev. A **79**, 042716 (2009).
[46] F. H. Mies, C. J. Williams, P. S. Julienne, and M. Kraus, J. Res. Natl. Inst. Stand. Technol. **101**, 521 (1996).
[47] See supplementary material at [http://link.aps.org/supplemental/10.1103/PhysRevA.82.052514].
[48] In brief, using a three level model, where the Rabi frequency Ω_2 is the only free parameter, we fit a line shape to the dark resonance [49].
[49] K. Winkler, F. Lang, G. Thalhammer, P. v. d. Straten, R. Grimm, and J. Hecker Denschlag, Phys. Rev. Lett. **98**, 043201 (2007).
[50] Three resonances reported by [19] were reassigned $l(m_A,m_B)$: 306.94 G to 2(0, 1), 1137.97 G to 3(−1, 1), and 729.43 G to 2(0, −1).